Research Article

Milica Hadnadjev-Kostic*, Djurdjica Karanovic, Tatjana Vulic, Jasmina Dostanić, and Davor Lončarević

Photocatalytic properties of ZnFe-mixed oxides synthesized via a simple route for water remediation

Abstract: ZnFe photocatalysts have been increasingly investigated for water remediation due to the high demands in this field, such as activity, toxicity, cost, and stability. The presented study was focused on the simple, safe, non-toxic, and eco-friendly synthesis and characterization of ZnFe-mixed metal oxides in correlation with their functional properties. Photocatalytic performance of these materials was evaluated by rhodamine B photodegradation under simulated solar light irradiation. The synthesized mixed oxides contained hexagonal wurtzite ZnO as the predominant phase, whereas, after thermal treatment, the formation of the spinel-structured $ZnFe_2O_4$ phase was observed. The photocatalysts with the additional spinel phase and thermally treated at 300°C and 500°C exhibited superior photocatalytic activity probably due to the highest amount of the $ZnFe_2O_4$ spinel phase, favourable mesoporous structure, and an optimal energy band gap of ~2.30 eV that initiated higher light-harvesting efficiency. The rhodamine B photodegradation followed zero-order kinetics, indicating complete coverage of active sites by the pollutant substrate. Additionally, photocatalysts showed the highest efficiency at the natural pH (6.8), being in accordance with green synthesis principles. Simple, green route assembling synthesis method, high photodegradation efficiency, and good reusability make these ZnFe-mixed oxides great candidates for potential application in practical wastewater treatments.

1 Introduction

The exponential increase of environmental pollution with no systematic solution has become an overwhelming concern in the scientific community [1]. As a consequence of the rapid growth of industrial regions, enormous amounts of wastewater are daily generated that represent a serious risk to the environment and human health [2,3]. Major organic pollutants are residual dyes from different industries, and considering their toxicity, unpleasant colouring, and non-biodegradation properties, these pollutants are sought to be extremely hazardous to the environment and capable of destroying aquatic organisms if present in water and/or wastewater [4–6]. In printing, textile, and photographic industries, organic dyes are frequently used and when released into the effluent water streams cannot usually be degraded without a catalytic assistance [7,8]. Rhodamine B (RhB), as a water-soluble, persistent synthetic cationic dye, is frequently employed in the industry and when released in wastewater, it is extremely difficult to be removed by physical methods considering its conjugations of aromatic rings (benzene, naphthalene) [9]. Therefore, effective removal methods present a challenging as well as motivating task that needs to be addressed with great precision in order to decrease or completely eliminate environmental problems regarding dye pollutants in wastewater [10]. Even though many processes have been developed, there is still an urgent need for further progress of removal processes that would fulfil all the requirements and would be simultaneously efficient and economically viable [1]. Numerous physical and chemical methods (adsorption, membrane filtration, electrolysis, sedimentation, coagulation, flocculation, chemical treatments, oxidation, biological treatments) have been reported for the removal of

---

* **Corresponding author: Milica Hadnadjev-Kostic,** Faculty of Technology Novi Sad, University of Novi Sad, Bul. Cara Lazara 1, 21000 Novi Sad, Serbia, e-mail: hadnadjev@uns.ac.rs, hadnadjev@tf.uns.ac.rs
Djurdjica Karanovic, Tatjana Vulic: Faculty of Technology Novi Sad, University of Novi Sad, Bul. Cara Lazara 1, 21000 Novi Sad, Serbia
Jasmina Dostanić, Davor Lončarević: Department of Catalysis and Chemical Engineering, Institute of Chemistry, Technology and Metallurgy, University of Belgrade, Njegoševa 12, 11000 Belgrade, Serbia

toxic molecules and bacteria from contaminated water [11]. Most of the mentioned methods have proven to have disadvantages in various aspects of applications and have the capability of only transferring harmful contaminants from one phase to another without decomposing toxic pollutants to nontoxic substances [11]. Various advanced oxidation processes have received much interest due to their high efficiency in degradation of chemical contaminations from wastewater, the most promising being photocatalysis, well known as a cost-effective and environmentally friendly method [12,13]. Considering that photocatalytic oxidation reactions are based on the free-radical reaction initiated by light irradiation of a photocatalyst (semiconductor) surface, the efficiency is influenced by various factors and depends on the mobility of electron–hole pairs as well as the accessibility of active sites on the surface of photocatalysts [1]. Moreover, due to the environmentally friendly process and consequent energy conservation with the use of solar light, semiconductor-based photocatalysis has recently become one of the most promising technologies in wastewater purification [4,6]. Taking into consideration that photocatalysis is a surface phenomenon, structural, textural, and optical properties of semiconductors mostly influence and determine their photocatalytic activity [1]. For efficient elimination of various pollutants, metal oxides, such as TiO_2, WO_3, CeO_2, and MnO_2, are frequently used as heterogeneous photocatalysts [14,15]. One of the most resourceful candidates in green environmental management has been zinc oxide (ZnO) because of its strong oxidation ability, good photocatalytic properties, and low cost [4,16,17]. Additional coupling of ZnO and a semiconductor with a narrow energy band gap would result in a more enhanced photocatalytic activity that could be a route to the efficient exploitation of the solar light source [12]. Mutual transfer of charge carriers, i.e. transfer of excited electrons from the conduction band of the narrow band gap semiconductor to the wide band gap semiconductor increases the photocatalytic performance [15]. Considering these advantages, mixed oxides are already widely used in heterogeneous catalysis because of their possibility to combine the properties of different metal oxides having different oxidation states, triggering the synergetic effect, increasing the number of lattice defects, and the number of active sites [5,18].

Inspired by the current research trend, in this study, ZnFe-mixed oxides were synthesized with the aim to induce solar-efficient photocatalytic properties. The chosen co-precipitation method has been emphasized as a robust, dependable, and time-saving process, without hazardous organic solvents, high-pressure or -temperature treatment and can be easily scaled-up for industrial applications [19,20]. In order to encourage sustainable processes and eliminate the use of toxic chemicals that are harmful to the environment, the motivation for this study was to apply the coprecipitation method in the synthesis path for ZnFe-mixed metal oxides that follows a simple, safe, nontoxic, eco-friendly, and cost-effective green route. Different thermal treatment/activation temperatures of synthesized materials were used to induce a variation in the crystallite size, energy band gap, and textural properties that influence photocatalytic activity in order to enhance photocatalytic performance in the rhodamine B photodegradation. Furthermore, in order to establish optimal reaction conditions and possible mechanism, stability, and pH influence of the most effective photocatalysts were also studied.

2 Materials and methods

2.1 Sample preparation

Mixed oxides (ZnFe-MO) were synthesized by a high supersaturation coprecipitation method with the use of 0.7 M $Zn(NO_3)_2 \cdot 6H_2O$ and 0.3 M $Fe(NO_3)_3 \cdot 9H_2O$ solution precursors that were added to the base solution (0.67 M Na_2CO_3 and 2.25 M NaOH) and vigorously stirred at a constant temperature (40°C). The precipitates were aged for 15 h and then washed with deionized water until pH 7 was reached. The schematic view of the synthesis path is presented in Figure 1. The products were dried for 24 h at 100°C (sample denoted as ZnFe100) and thermally treated for 5 h at different temperatures in the air: 300°C, 500°C, 700°C, and 900°C (samples denoted as ZnFe300, ZnFe500, ZnFe700, and ZnFe900, respectively).

2.2 Characterization

X-ray powder diffraction (XRD) was used for the interpretation of the phase composition. The analysis was conducted using a Rigaku MiniFlex 600 with Cu-Kα radiation, wavelength of $\lambda = 0.15406$ nm, at 40 kV and 40 mA in the 2θ range from 10° to 80° and angular steps of 0.02° with a step time of 3 s. The crystallite sizes were calculated using the Scherrer formula and the full-width at half-maximum (FWHM) of the most intense diffraction peak (Eq. 1):
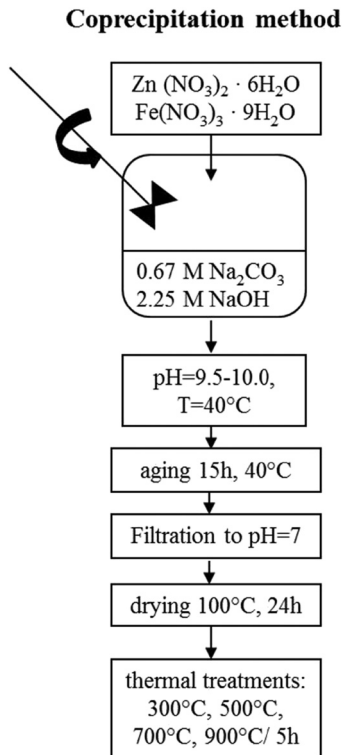
$$D = k\frac{\lambda}{\beta\cos\theta} \qquad (1)$$

Coprecipitation method

Figure 1: Schematic representation of the co-precipitation synthesis path followed by the thermal treatment.

where D is the crystallite size (nm), k is the shape function (0.9), λ is the X-ray wavelength, θ is the angle of diffraction, and β is the FWHM of the considered peak.

The Fourier transform infrared spectroscopy (FTIR) spectra of the powdered samples were recorded using an Alpha FTIR spectrometer (BRUKER Optics, Germany). The FTIR spectra were recorded with a spectral resolution of $4\,cm^{-1}$ in the range of $4{,}000{-}400\,cm^{-1}$ with 24 averaged scans per measurement.

The morphology of samples was investigated with a scanning electron microscope (SEM, Hitachi, TM3030).

The texture of samples was analysed by low-temperature nitrogen adsorption at –196°C (Micromeritics ASAP 2000). The surface area of the samples was calculated by the Brunauer–Emmett–Teller (BET) method. The pore size distribution and the cumulative pore volume were determined by the Brunauer–Joyner–Halenda (BJH) method applied to the desorption branch of the isotherm.

The energy band gap, E_g, of samples was calculated by applying the Tauc plot as a direct allowed transition function to diffuse reflectance spectra (DRS). DR UV-Vis spectra were recorded on a Nicolet Evolution 500 spectrometer, with a diffuse reflectance accessory (Thermo Electron Corporation).

2.3 Photocatalytic degradation of rhodamine B

Photocatalytic tests were performed in an open cylindrical thermostatic Pyrex reaction vessel using an Osram Ultra Vitalux 300 W lamp with the emission spectrum that simulates solar light, housed 45 cm above the top surface of the dye solution. The suspensions were exposed to air without additional aeration throughout the duration of each experiment. The photocatalytic efficiency of all the prepared samples was estimated by RhB photodegradation, monitoring the decrease of RhB concentration with time. In order to ensure the required adsorption/desorption equilibrium between the RhB dye and the catalyst surface, the reaction mixtures (50 mg of catalysts and 100 mL of $4.8\,mg{\cdot}L^{-1}$ RhB solution) were stirred in the dark for 30 min, before exposure to light. When the equilibrium was established, reaction mixtures were irradiated with light and aliquots were analysed at defined time intervals using an UV-Vis spectrophotometer. Prior to the reaction on active sites, the first step of every heterogeneous catalytic reaction is the adsorption of reactive species on the catalysts' surface. In order to evaluate only the photocatalytic efficiency and eliminate any possible adsorption that is not related to the photocatalytic reaction, blank samples (reaction solution with the catalyst) were retained in the dark, and the RhB concentration was measured at the defined time intervals. The photodegradation efficiency was estimated by the RhB photodegradation and calculated based on the total conversion using the following equation:

$$\text{Photodegradation efficiency (\%)} = \frac{C_0 - C_t}{C_0} \times 100 \quad (2)$$

where C_0 is the RhB concentration of the blank sample and C_t is the RhB concentration of irradiated samples, both measured at defined time intervals. The RhB concentration was measured by UV-Vis spectrophotometry (EVOLUTION 600 spectrophotometer) at $\lambda = 554$ nm.

An inductively coupled plasma optical emission spectrometer (ICP–OES), iCAP 6500 Duo ICP (Thermo Fisher Scientific) was used to quantify the potential leaching of Zn^{2+} ions from the catalyst after the photocatalytic test.

2.4 Kinetics of the RhB photocatalytic reaction

In order to investigate the data obtained during the photodegradation process, the zero-order kinetic model was used to describe the photocatalytic kinetic process (Eq. 3):
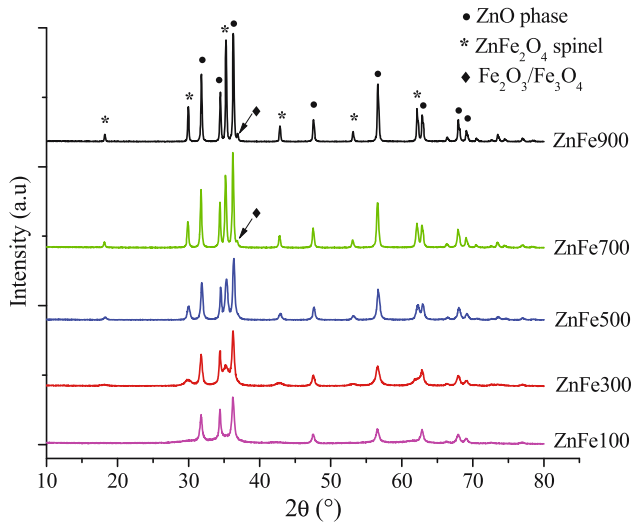
Figure 2: XRD diffraction peaks of thermally treated samples ZnFe100, ZnFe300, ZnFe500, ZnFe700, and ZnFe900 at different temperatures.

$$C_t = C_0 - k \cdot t \qquad (3)$$

where C_0 and C_t are initial and reaction time (t) concentrations and k is the zero-order rate constant [21,22].

3 Results and discussion

3.1 Structural properties

XRD diffraction peaks of all synthesized and thermally treated photocatalysts are presented in Figure 2 and can be correlated with the series of Bragg reflections corresponding to the standard JCPDS. In the sample ZnFe100, sharp intense diffraction peaks were observed at 31.8°, 34.4°, 36.2°, 47.5°, 56.6°, 62.8°, and 68.0° that correspond to (100), (002), (101), (102), (110), (103), and (112) crystalline lattice, respectively, for the ZnO phase (JCPDS File no. 79-2205) [23,24]. These results imply that the phase composition of as-synthesized materials was ZnFe-mixed oxide

phase with predominant properties of the wurzite ZnO phase.

It was observed that the crystallinity increased upon increase of the thermal treatment temperature. Additional diffraction patterns were detected for thermally treated samples with sharp intense peaks at 0.05°, 35.4°, 42.8°, 53°, 56.8°, and 62.2° that correspond to the spinel phase $ZnFe_2O_4$ with (220), (311), (400), (422), (511), and (440) crystalline lattice, respectively (JCPDS File no. 89-1012) [25]. Previous reports suggested that for ZnFe samples at low temperatures (<400°C), only the ZnFe-mixed oxide phase with predominant properties of the wurzite ZnO phase can be distinguished, whereas higher thermal activation temperatures trigger the formation of an additional $ZnFe_2O_4$ spinel phase [26]. The presented XRD results are in accordance with these findings where, at temperatures higher than 300°C, the formation of the $ZnFe_2O_4$ spinel was pronounced, whereas XRD patterns at 300°C showed a slight, but not evident, beginning of this phase formation. Additionally, with the increase in the thermal treatment temperature, the amount of the $ZnFe_2O_4$ phase with the cubic structure also increased. Furthermore, in samples thermally treated at 700°C and 900°C, a low-intense peak (at $2\theta = 37°$) was noticed that could be assigned to the presence of either the Fe_2O_3 or Fe_3O_4 phase in accordance with JCPDS (File no. 87-2334) [27]. The calculated crystallite sizes of all samples, presented in Table 1, showed that the crystallite size increased with an increase in the temperature of thermal treatment, since the temperature increase results in the grain growth triggering a greater crystallite size [26,28].

FTIR spectroscopy was conducted in order to gain more information on the structure, composition, and functional groups of the synthesized and thermally treated samples. The FTIR spectra of all samples are shown in Figure 3a. Broad bands detected at ~3,430 and ~1,630 cm^{-1} in ZnFe100 were attributed to bending and stretching vibrations of O–H bonds, respectively, due to water molecules adsorbed on the surface of ZnFe100 that was still present after the thermal treatment at 100°C [5,11,13]. In FTIR spectra of

Table 1: Crystallite size, textural properties, energy band, and kinetic parameters for all investigated mixed oxides

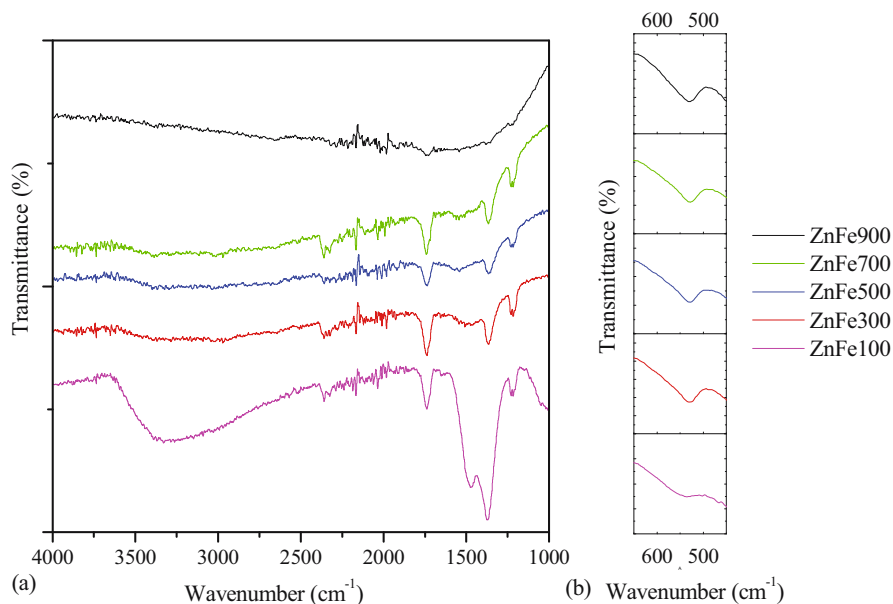| Sample	Crystallite size (nm)	2θ for crystallite size	BET surface area (m²·g⁻¹)	Average pore diameter (nm)	Energy band (eV)	Rate constant (mg·L⁻¹·min⁻¹)	Correlation coefficient R^2 (−)
ZnFe-100	20.7	36.2	110	6.8	2.27	0.0089	0.9886
ZnFe-300	22.4	36.3	46	12	2.29	0.0173	0.9979
ZnFe-500	25.5	36.4	16	27.6	2.31	0.0174	0.981
ZnFe-700	33.7	36.2	9	18.2	2.27	0.0135	0.982
ZnFe-900	41.3	36.3	3	12.8	2.14	—	—

Figure 3: FTIR spectra of ZnFe100, ZnFe300, ZnFe500, ZnFe700, and ZnFe900 in the spectral range from (a) 4,000 to 1,000 cm^{-1} and (b) 650 to 450 cm^{-1}.

ZnFe300, ZnFe500, ZnFe700, and ZnFe900 samples, no bands around 3,400 and 1,630 cm^{-1} were detected that indicated the absence of any OH vibrations of water molecules. Furthermore, three bands at 1,471, 1,365, and 1,205 cm^{-1} were distinguished in all samples and could be attributed to C–O stretching, confirming the presence of carbonate species that decreased with the increase of the thermal treatment temperature [13,18]. The bands in the range of 400–800 cm^{-1} can be considered as lattice vibration modes of metal–OH and metal–oxygen (M–O) [11]. Figure 3b is presented to distinguish the FTIR bands in the mentioned spectral region. All samples with the exception of ZnFe100 revealed distinct vibration band for M–O at ~530 cm^{-1} that could reflect the stretching vibration of the M–O bond in the ZnFe$_2$O$_4$ spinel related to the metal cations at the octahedral sites of the spinel lattice [29]. This vibration band was also detected in the ZnFe100 sample but considering the broad and low intensive peaks it can be concluded that the

presence of the ZnFe$_2$O$_4$ phase was low. The obtained FTIR results were in accordance with the XRD analysis.

3.2 Morphological properties

SEM images of the investigated samples are shown in Figure 4. As observed from the images, the ZnFe samples had the same morphology indicating the formation of large particles with irregular shapes [15] that are aggregates of very small ones [18]. A slightly different morphology was detected for the ZnFe900 sample that demonstrated a similar surface morphology but with larger compact aggregates of more spherical particles. From the obtained SEM results, it can be concluded that compared to other samples, the ZnFe900 sample formed agglomerations of organized, uniformly sized spherical particles that could most
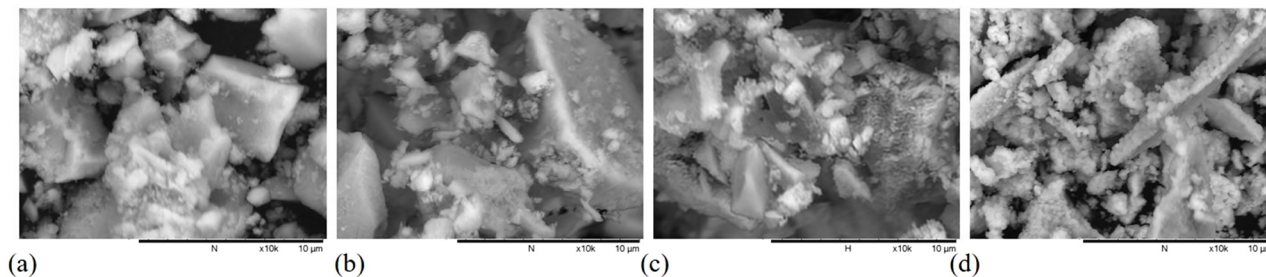

Figure 4: SEM images of (a) ZnFe100, (b) ZnFe500, (c) ZnFe700, and (d) ZnFe900.

probably have been triggered by higher crystallinity observed by the XRD analysis [5].

3.3 Textural properties: Surface area and pore size distribution

The textural analysis results are presented in Table 1 and Figure 5. According to the experimental data, the isotherms of all samples could be associated with type IV with a combined H1/H3 hysteresis loop, clearly suggesting that all investigated samples have mesoporous structures (Figure 5a).

Furthermore, the formation of a hysteresis loop at a higher relative pressure (P/P_0) in the range of 0.4–1.00 directly indicated that the mesopores are non-uniform in all investigated photocatalysts [30]. As expected, the surface area of samples decreased with the increase of the thermal treatment temperature due to the decrease of smaller mesopores, particularly obvious for the ZnFe900 sample. The ZnFe100 sample revealed a developed pore size distribution with two peaks: an intense peak at ~3 nm and a broad peak at ~30 nm. Upon thermal treatment, the presence of pores with diameters ~3 nm decreased and completely disappeared in samples thermally treated at temperatures above 500°C (Figure 5b). Additionally, a higher presence of larger mesopores (~30 nm) was observed in ZnFe300 and ZnFe500 samples, which also gradually disappeared with the temperature increase in ZnFe700 and ZnFe900 samples, being in correlation with the calculated pore volume of samples (Table 1).

3.4 Optical properties

The UV-Vis DRS were applied for energy band gap determination (E_g) using the Kubelka–Munk transformation. The reflectance spectra and the plot $F(R)^2$ as a function of E_g for the investigated samples are presented in Figure 6. The calculated data for E_g for direct transition are presented in Table 1.

The results showed that there was no significant difference in E_g among investigated samples, ranging from 2.14 to 2.31 eV. The determined E_g corresponds to visible light energy. A slightly lower E_g achieved for the samples ZnFe900 is likely a consequence of the Fe_2O_3/Fe_3O_4 phase formation [4,15].

3.5 Photocatalytic performance

The investigation of photocatalytic efficiency was conducted at room temperature using solar light source radiation (Figure 7). Prior to illumination, the RhB photodegradation without catalysts (photolysis experiments) was also monitored and the results indicated that the RhB pollutant was stable and could not be degraded solely by solar light [31,32]. Additional adsorption measurements were carried out in the dark in the presence of photocatalysts (Figure 7a). Based on these experiments, the RhB concentration did not significantly change during the 90 min dark reaction. Moreover, it can be clearly seen
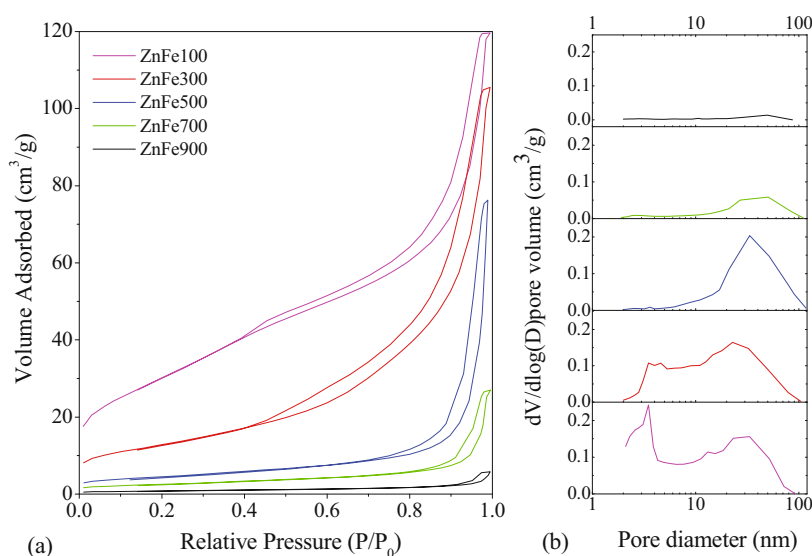
Figure 5: Textural analysis of all investigated photocatalysts: (a) nitrogen adsorption–desorption isotherm curves and (b) BJH pore size distribution curves.
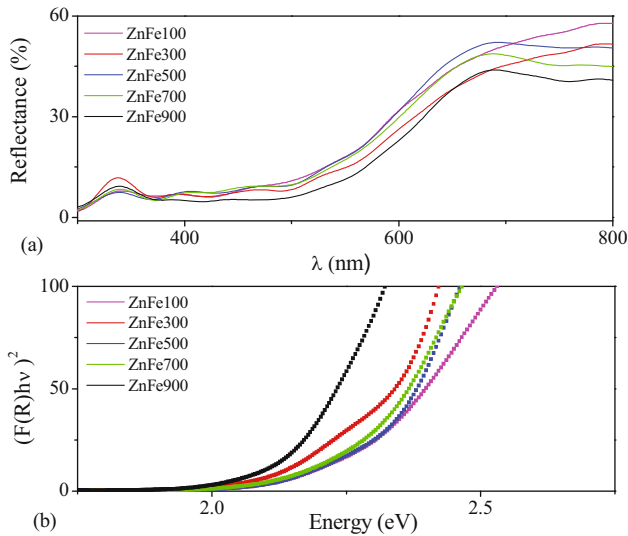
Figure 6: Optical measurements for all samples: (a) UV-Vis DRS and (b) Tauc plot for the determination of the energy band gap.

that the adsorption equilibrium was reached after 30 min dark reaction. These results further confirmed that the photocatalytic performance of the samples was attributed only to the photocatalytic reaction, eliminating the possibility of self-degradation and adsorption of RhB solution. The results demonstrated that both photocatalyst and light were required for effective RhB dye degradation.

The photocatalytic efficiency of ZnFe samples in RhB photodegradation is presented in Figure 7b. All samples that were thermally treated at temperatures lower than 900°C were active in the RhB photodegradation reaction, whereas the sample ZnFe900 did not show any photocatalytic activity.
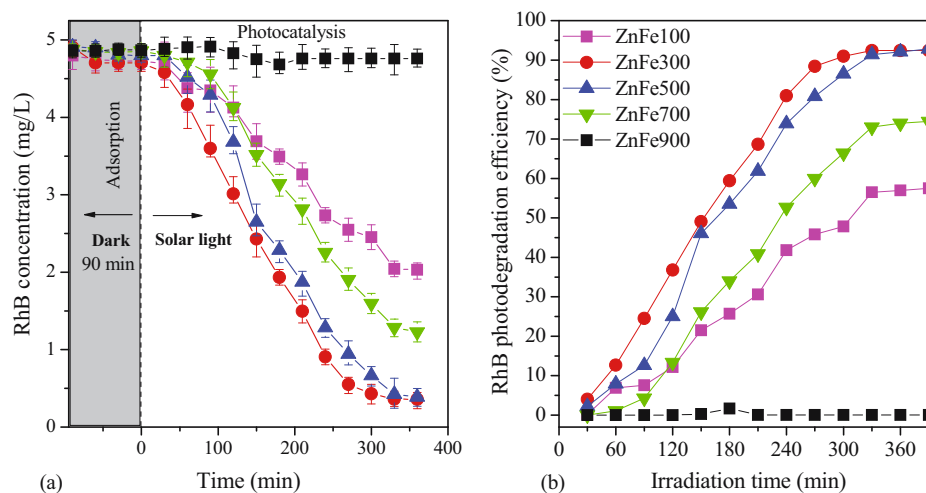
The samples ZnFe300 and ZnFe500 showed the highest photocatalytic efficiency. When compared to the as-synthesized ZnFe100 sample, the thermal treatment at 300°C and 500°C elevated the photodegradation efficiency significantly. On the contrary, with higher thermal treatment temperatures (700°C and 900°C), the photodegradation efficiency declined probably due to the sintering process that occurred in these samples and could be suggested based on their specific surface areas that were drastically low (9 $m^2 \cdot g^{-1}$ for ZnFe700 and 3 $m^2 \cdot g^{-1}$ for ZnFe900). These findings are in accordance with previous studies that stated that insufficient photocatalytic performance can be directly related to their poor textural properties such as low surface area and agglomeration [21,22]. The enhanced photocatalytic activity could be additionally explained by the structural, textural, and optical properties. The explanation for the highest photocatalytic activity of ZnFe300 and ZnFe500 could be due to the presence of the highest amount of the $ZnFe_2O_4$ spinel phase. Considering that with a further temperature increase, an additional Fe_2O_3 phase was detected that negatively affected the photocatalytic performances due to the fact that the Fe_2O_3 phase could act as a charge carrier centre [5]. Additionally, the mesoporous structure of ZnFe300 and ZnFe500 could be beneficial for the adsorption of dye molecules, causing higher photodegradation efficiency. In these samples, the coupling of ZnO and $ZnFe_2O_4$ phases resulted in energy bands (from 2.1 to 2.3 eV) that elevated the photodegradation in the solar light spectrum. It was reported that the single $ZnFe_2O_4$ phase exhibited significantly lower optical band gap (1.9 eV) when compared to pure ZnO (~3.1 eV) [30,33]. The energy band gap for the

Figure 7: Photocatalytic tests of ZnFe samples: (a) pre-adsorption measurement of RhB in the dark, followed by RhB photodegradation and (b) photocatalytic efficiency.

most active samples was ~2.3 eV, which initiated stronger absorption of light-enabling photogenerated electrons (e^-) to facilely transfer between $ZnFe_2O_4$ and ZnO and prevent the e^-/h^+ recombination. Therefore, in general, the photocatalytic performance of photocatalysts under the same irradiation conditions depends on the photoabsorption ability, the surface reaction between photogenerated carriers and surface adsorbed reactants, and the rate of e^-/h^+ recombination [22].

3.6 Kinetic studies

The results of the kinetic study indicated that the photodegradation of RhB dye follows the zero-order reaction model (Figure 8 and Table 1). Even though previously published studies suggested that the kinetics of organic dye photodegradation can be described with the pseudo-first-order model, recent studies indicated that zero-order kinetics was satisfactory in describing these photocatalytic reactions [34]. The photocatalytic degradation of dye follows the zero-order rate due to (i) the photocatalysts' surface saturation with organic reactants and/or (ii) the reaction limitation by other participants (electron transfer to O_2, oxygen mass transfer, or light supply) [34–36].

3.7 Photodegradation mechanism study

When a photocatalyst is irradiated by light with energy greater than the photocatalyst band gap, the valence band holes (h_{VB}^+) and conduction band electrons (e_{CB}^-) are generated. Depending on their oxidation, i.e. reduction power,

h_{VB}^+ and e_{CB}^- can initiate a wide range of chemical reactions. The holes can directly oxidize the pollutant dye or react with OH^- or H_2O, oxidizing them to ˙OH radicals. Furthermore, the photogenerated e_{CB}^- can directly reduce the pollutant molecule or react with O_2, reducing them to the superoxide radical anion ˙O_2^-. Therefore, the most important reactive species are e_{CB}^-, h_{VB}^+, hydroxyl (˙OH), and superoxide (˙O_2^-) radicals. The contribution of each reactive species in the photocatalytic reaction depends not only on the pollutant chemical properties but also on the type of the used photocatalyst. It was reported that both photogenerated ˙O_2^- and holes played a critical role in the dye photodegradation using the ZnO/In_2O_3 composite as a photocatalyst [37]. Additionally, ˙OH radicals are found to be the main reactive species in the photodegradation of methylene blue using Au cube-ZnO core–shell nanoparticles [38]. The RhB photodegradation using Ag nanoparticles-decorated ZnO microspheres was found to proceed mainly through the ˙OH radical mechanism [39]. ZnO/Co_3O_4 hetero-nanostructures were applied for methylene blue removal, and the results showed that the use of ammonium oxalate as hole scavenger increased the degradation efficiency, while the presence of silver nitrate as an electron scavenger diminished the removal efficiency, concluding that both electrons and holes take part in dye photodegradation [40]. Among the active species trapping experiments, LC-MS/MS analysis [41] and DFT calculations [42] were also used as successful tools to elucidate the photodegradation mechanism. Using DFT calculations, the authors found that the nitrogen atoms are the sites most susceptible to the radical attack, followed by tertiary cyclo-carbon atoms in RhB photodegradation with Pd-modified
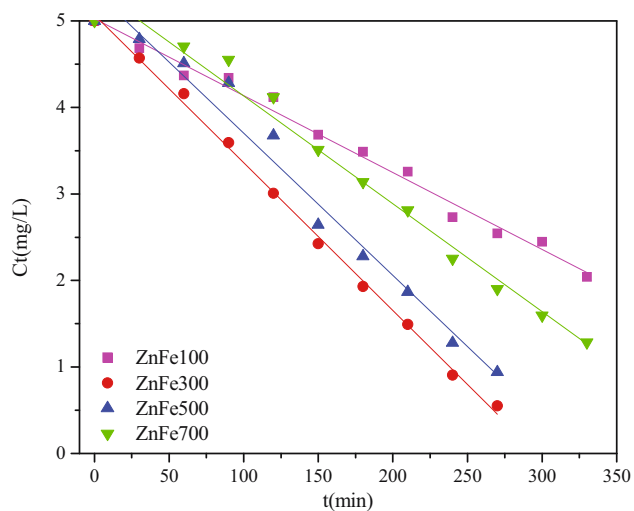

Figure 8: Photocatalytic degradation zero-order kinetic model (the solid lines show linear fitting for the zero-order kinetic model).
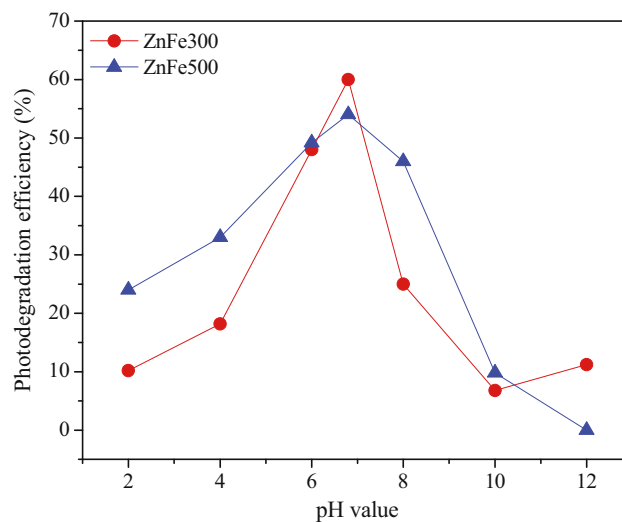

Figure 9: Effect of pH on the RhB photodegradation efficiency in the presence of ZnFe300 and ZnFe500.

TiO_2/Bi_2O_3 as a photocatalyst [42]. The results from LC-MS analysis showed that the mineralization of RhB dye proceeds via de-ethylation, chromophore cleavage, ring-opening, and fragmentation [42]. According to a recent study [41], there are two possible RhB photodegradation pathways. In the first proposed mechanism, following the ˙OH radical attack, de-ethylated product of RhB is formed, after which de-amination and ring opening occur, leading to the formation of hydroquinone and further smaller molecules. The second proposed mechanism suggests that the positive amino group of the RhB molecule is first attacked by $˙O_2^{-}$, leading to the elimination of the benzoic acid moiety and formation of the 3,9a-dihydroxanthen-9-one structure with nitro and amino groups, which further decomposed to resorcinol and smaller molecules.

3.8 Effect of pH

The photodegradation efficiency can be strongly influenced by pH variations due to surface charge changes.

The effect of pH on photodegradation efficiency can be explained by the following: (i) the dye adsorption on photocatalyst surfaces is affected by pH variations, (ii) the concentration and formation rate of hydroxyl radicals are enhanced in alkaline media; therefore, the number of hydroxide ions available on surfaces are different from acidified solution, and (iii) pH-dependent agglomeration indirectly affects the available surface area for dye adsorption and photon absorption [1,43]. In order to investigate the effect of the initial pH of reaction solutions on the RhB photodegradation efficiency, photocatalytic tests were conducted in the pH range from 2 to 12 for the most efficient photocatalysts (ZnFe300 and ZnFe500). Aqueous solutions of HCl and NaOH were added for adjusting the initial pH and the results are shown after 180 min of solar light irradiation (Figure 9). The initial pH of the RhB solution with photocatalysts was 6.8. It can be observed that the highest efficiency for both the studied photocatalysts was reached at an initial pH of 6.8. Considering that RhB is a cationic dye, the adsorption of cationic species is favoured close to neutral and alkaline pH solutions that initiate negatively charged surfaces of
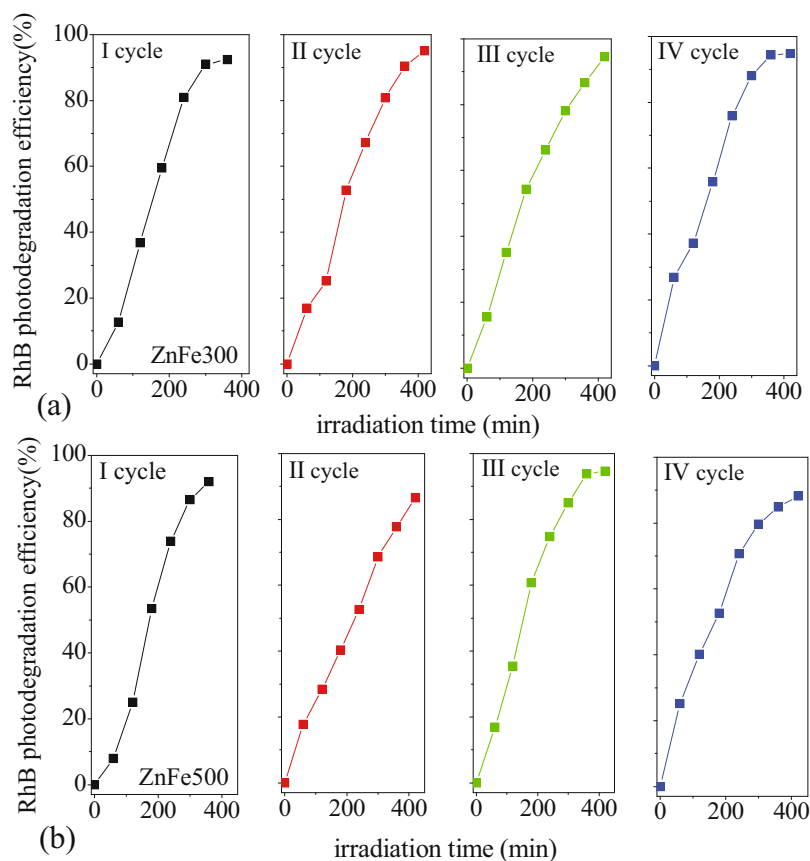

Figure 10: Stability tests for (a) ZnFe300 and (b) ZnFe500 samples for RhB photodegradation under solar light irradiation.

photocatalysts. On the contrary, low pH values trigger positively charged surfaces preventing the adsorption of the RhB cationic dye and acting as repulsive forces towards cationic dyes [1,43].

These findings are in agreement with other studies, where the optimum working condition for the photodegradation of cationic dyes was pH 7 [9]. Furthermore, the presented results are correlated with the green route intentions where the highest photodegradation efficiency was achieved without any additional adjustment or use of chemicals.

3.9 Stability test

Since the catalysts ZnFe300 and ZnFe500 exhibited the highest efficiency, stability tests were conducted on these photocatalysts. In order to determine the photocatalytic stability, four consecutive photodegradation cycles for RhB were performed under the same operating conditions (Figure 10). For the ZnFe300 photocatalyst, it was observed that after four cycles of consecutive decomposition reactions, there was no reduction in the catalyst efficiency (Figure 10a). The ZnFe500 photocatalyst showed similar photostability as the ZnFe300 catalyst with no significant loss after four consecutive reaction cycles (Figure 10b).

From these analyses, it can be concluded that the stability of these photocatalysts was high and satisfactory, and thus they meet one of the many conditions for their applications in environmental protection in wastewater treatment.

After stability experiments, a leaching test was performed to determine the release of Zn from the ZnFe500 photocatalyst. The results showed that the Zn content after the photocatalytic test was $4.9\,mg\cdot L^{-1}$, which is below the permissible limits for drinking water (Public Health Service Agency for Toxic Substances and Disease Registry, Public Health Statement, CAS#: 7440-66-6). The detected slight leaching of Zn ions from the photocatalysts after the stability tests could be responsible for the loss of active sites, resulting in a slight reduction of photodegradation efficiency in the presented sample [44].

4 Conclusions

The photocatalytic efficiency of the eco-friendly synthesized Zn/Fe mixed oxides was evaluated in degradation of the cationic RhB dye. The synthesized mixed oxides contained hexagonal wurtzite ZnO as the predominant phase. The thermal treatment led to the formation of the additional $ZnFe_2O_4$ spinel phase, while the presence of either the Fe_2O_3 or Fe_3O_4 phase was observed in photocatalysts thermally treated at 700°C and 900°C. Textural analysis revealed mesoporous structures in all mixed oxides with non-uniform mesopores, as well as a decrease in the surface area with the increase of the thermal treatment temperature. Investigation of optical properties showed energy band gaps that proved the advantages of mixed oxides synthesis, having narrow bands (from 2.14 to 2.31 eV) when compared to the pure ZnO photocatalyst. The photocatalytic results revealed that ZnFe300 and ZnFe500 mixed oxides exhibited the highest photocatalytic efficiency, probably due to the highest amount of the $ZnFe_2O_4$ spinel phase, mesoporous structure, and the optimal energy band gap of ~2.30 eV that initiated higher light-harvesting efficiency. The RhB photodegradation followed zero-order kinetics, indicating complete coverage of active sites by the RhB substrate. The photocatalysts showed the highest efficiency at the natural pH (6.8), in accordance with green synthesis principles. ZnFe300 and ZnFe500 photocatalysts showed high stability with negligible leaching of Zn^{2+} ions, indicating their potential application in environmental protection processes. The results demonstrated that the developed simple, safe, non-toxic, eco-friendly, and cost-effective synthesis method enabled favourable interactions among active phases triggering excellent photocatalytic performance making these photocatalysts suitable for use in wastewater remediation.

Author contributions: Milica Hadnadjev-Kostic: writing – original draft, conceptualization, methodology, investigation, formal analysis, data curation, validation; Djurdjica Karanovic: formal analysis, data curation, validation; Tatjana Vulic: writing – review and editing, conceptualization, validation; Jasmina Dostanić: formal analysis, data curation; Davor Lončarević: formal analysis, data curation. All authors have read and agreed to the published version of the manuscript.

Conflict of interest: The authors state no conflict of interest.

Data availability statement: All relevant data are within the article.

References

[1]   Hadnadjev-Kostic M, Vulic T, Marinkovic-Neducin R, Lončarević D, Dostanić J, Markov S, et al. Photo-induced properties of photocatalysts: A study on the modified structural, optical and textural properties of TiO₂–ZnAl layered double hydroxide based materials. J Clean Prod. 2017;164:1–18. doi: 10.1016/j.jclepro.2017.06.091.

[2]   Nguyen LTT, Vo DVN, Nguyen LTH, Duong ATT, Nguyen HQ, Chu NM, et al. Synthesis, characterization, and application of ZnFe₂O₄@ZnO nanoparticles for photocatalytic degradation of Rhodamine B under visible-light illumination. Env Technol Innov. 2022;25:102130. doi: 10.1016/j.eti.2021.102130.

[3]   Hadnadjev-Kostic M, Vulic T, Marinkovic-Neducin R. Solar light induced rhodamine B degradation assisted by TiO₂-Zn-Al LDH based photocatalysts. Adv Powder Technol. 2014;25(5):1624–33. doi: 10.1016/j.apt.2014.05.015.

[4]   Yang Q, Wang S, Chen F, Luo K, Sun J, Gong C, et al. Enhanced visible-light-driven photocatalytic removal of refractory pollutants by Zn/Fe mixed metal oxide derived from layered double hydroxide. Catal Commun. 2017;99:15–9. doi: 10.1016/j.catcom.2017.05.010.

[5]   Bayahia H. High activity of ZnFe₂O₄ nanoparticles for photodegradation of crystal violet dye solution in the presence of sunlight. J Taibah Univ Sci. 2022;16:988–1004. doi: 10.1080/16583655.2022.2134696.

[6]   Labhane PK, Sonawane GH, Sonawane SH. Influence of rare-earth metal on the zinc oxide nanostructures: Application in the photocatalytic degradation of methylene blue and p-nitro phenol. Green Process Synth. 2018;7(4):360–71. doi: 10.1515/gps-2017-0006.

[7]   Hadnađev-Kostić MS, Vulić TJ, Karanović ĐM, Milanović MM. Advanced dye removal by multifunctional layered double hydroxide based materials: Adsorption and kinetic studies. J Serb Chem Soc. 2022;87(9):1011–24. doi: 10.2298/JSC220228034H.

[8]   Zhou X, Yang H, Wang C, Mao X, Wang Y, Yang Y, et al. Visible light induced photocatalytic degradation of rhodamine B on one-Dimensional iron oxide particles. J Phys Chem C. 2010;114(40):17051–61. doi: 10.1021/jp103816e.

[9]   Le AT, Samsuddin NSB, Chiam S-L, Pung S-Y. Synergistic effect of pH solution and photocorrosion of ZnO particles on the photocatalytic degradation of Rhodamine B. B Mater Sci. 2021;44:5. doi: 10.1007/s12034-020-02281-6.

[10] Zhang D. Synergetic effects of Cu₂O photocatalyst with titania and enhanced photoactivity under visible irradiation. Acta Chim Slov. 2013;6(1):141–9. doi: 10.2478/acs-2013-0022.

[11] Zhao G, Liu L, Li C, Zhang T, Yan T, Yu J, et al. Construction of diatomite/ZnFe layered double hydroxides hybrid composites for enhanced photocatalytic degradation of organic pollutants. J Photochem Photobiol A. 2018;367:302–11. doi: 10.1016/j.jphotochem.2018.08.048.

[12] Jaffri SB, Ahmad KS. Foliar-mediated Ag:ZnO nanophotocatalysts: Green synthesis, characterization, pollutants degradation, and in vitro biocidal activity. Green Process Synth. 2019;8(1):172–82. doi: 10.1515/gps-2018-0058.

[13] Shakil M, Inayat U, Ashraf M, Tanveer M, Gillani SSA, Dahshan A. Photocatalytic performance of novel zinc ferrite/copper sulfide composites for the degradation of Rhodamine B dye from wastewater using visible spectrum. Opt (Stuttg). 2023;272:170353. doi: 10.1016/j.ijleo.2022.170353.

[14] Pradhan GK, Martha S, Parida KM. Synthesis of multifunctional nanostructured zinc-iron mixed oxide photocatalyst by a simple solution-combustion technique. ACS Appl Mater Interfaces. 2012;4(2):707–13. doi: 10.1021/am201326b.

[15] Dhal JP, Mishra BG, Hota G. Hydrothermal synthesis and enhanced photocatalytic activity of ternary Fe₂O₃/ZnFe₂O₄/ZnO nanocomposite through cascade electron transfer. RSC Adv. 2015;5:58072–83. doi: 10.1039/c5ra05894e.

[16] Fang B, Xing Z, Sun D, Li Z, Zhou W. Hollow semiconductor photocatalysts for solar energy conversion. APM. 2022;1(2):100021. doi: 10.1016/j.apmate.2021.11.008.

[17] Chani MTS, Khan SB, Rahman MM, Kamal T, Asiri AM. Sunlight assisted photocatalytic dye degradation using zinc and iron based mixed metal-oxides nanopowders. J King Saud Univ Sci. 2022;34(3):101841. doi: 10.1016/j.jksus.2022.101841.

[18] Florent M, Giannakoudakis DA, Wallace R, Bandosz TJ. Mixed CuFe and ZnFe (hydr)oxides as reactive adsorbents of chemical warfare agent surrogates. J Hazard Mater. 2017;329:141–9. doi: 10.1016/j.jhazmat.2017.01.036.

[19] Cruz IF, Freire C, Araújo JP, Pereira C, Pereira AM. Multifunctional ferrite nanoparticles: from current trends toward the future. Magnetic Nanostructured Materials: From Lab to Fab. Amsterdam, The Netherlands: Elsevier; 2018. p. 59–116. doi: 10.1016/B978-0-12-813904-2.00003-6.

[20] Letifi H, Dridi D, Litaiem Y, Ammar S, Dimassi W, Chtourou R. High efficient and cost effective titanium doped tin dioxide based photocatalysts synthesized via co-precipitation approach. Catalysts. 2021;11(7):803. doi: 10.3390/catal11070803.

[21] Mohtar SS, Aziz F, Ismail AF, Sambudi NS, Abdullah H, Rosli AN, et al. Catalysts impact of doping and additive applications on photocatalyst textural properties in removing organic pollutants: A review. Catalysts. 2021;11(10):1160. doi: 10.3390/catal.

[22] Amano F, Nogami K, Tanaka M, Ohtani B. Correlation between surface area and photocatalytic activity for acetaldehyde decomposition over bismuth tungstate particles with a hierarchical structure. Langmuir. 2010;26(10):7174–80. doi: 10.1021/la904274c.

[23] Devi PG, Velu AS. Synthesis, structural and optical properties of pure ZnO and Co doped ZnO nanoparticles prepared by the co-precipitation method. J Theor Appl Phys. 2016;10:233–40. doi: 10.1007/s40094-016-0221-0.

[24] Kalpanadevi K, Sinduja CR, Manimekalai R. Characterisation of zinc oxide and cadmium oxide nanostructures obtained from the low temperature thermal decomposition of inorganic precursors. ISRN Inorg Chem. 2013;2013:823040. doi: 10.1155/2013/823040.

[25] Anchieta C, Cancelier A, Mazutti M, Jahn S, Kuhn R, Gündel A, et al. Effects of solvent diols on the synthesis of ZnFe₂O₄ particles and their use as heterogeneous photo-fenton catalysts. Materials. 2014;7(9):6281–90. doi: 10.3390/ma7096281.

[26] Kim BK, Lee DY, Gwak GH, Han YS, Oh JM. Zn-Fe mixed metal oxides from metal hydroxide precursor: Effect of calcination temperature on phase evolution, porosity, and catalytic acidity. J Solid State Chem. 2019;269:454–8. doi: 10.1016/j.jssc.2018.10.013.

[27] Liu X, Zhu F, Wang W, Lei J, Yin G. Synthesis of single-crystalline iron oxide magnetic nanorings as electrochemical biosensor for dopamine detection. Int J Electrochem Sci. 2016;11:9696–703. doi: 10.20964/2016.11.62.

[28] Afzal A, Mujahid A, Iqbal N, Javaid R, Qazi UY. Enhanced high-temperature (600°C) NO_2 response of $ZnFe_2O_4$ nanoparticle-based exhaust gas sensors. Nanomaterials. 2020;10(11):1–14. doi: 10.3390/nano10112133.

[29] Nguyen-Phu H, Do LT, Shin EW. Investigation of glycerolysis of urea over various ZnMeO (Me = Co, Cr, and Fe) mixed oxide catalysts. Catal Today. 2020;352:80–7. doi: 10.1016/j.cattod.2019.09.017.

[30] Cai C, Zhang Z, Liu J, Shan N, Zhang H, Dionysiou DD. Visible light-assisted heterogeneous Fenton with $ZnFe_2O_4$ for the degradation of Orange II in water. Appl Catal B. 2016;182:456–68. doi: 10.1016/j.apcatb.2015.09.056.

[31] Yang L, Liu B, Liu T, Ma X, Li H, Yin S, et al. A P25/$(NH_4)xWO_3$ hybrid photocatalyst with broad spectrum photocatalytic properties under UV, visible, and near-infrared irradiation. Sci Rep. 2017;7:45715. doi: 10.1038/srep45715.

[32] Khalid NR, Mazia U, Tahir MB, Niaz NA, Javid MA. Photocatalytic degradation of RhB from an aqueous solution using Ag_3PO_4/N-TiO_2 heterostructure. J Mol Liq. 2020;313:113522. doi: 10.1016/j.molliq.2020.113522.

[33] Sun S, Yang X, Zhang Y, Zhang F, Ding J, Bao J, et al. Enhanced photocatalytic activity of sponge-like $ZnFe_2O_4$ synthesized by solution combustion method. Prog Nat Sci Mater. 2012;22(6):639–43. doi: 10.1016/j.pnsc.2012.11.008.

[34] Ollis DF. Kinetics of photocatalyzed reactions: Five lessons learned. Front Chem. 2018;6:378. doi: 10.3389/fchem.2018.00378.

[35] Murzin DY. On Langmuir kinetics and zero order reactions. Catal Commun. 2008;9(9):1815–6. doi: 10.1016/j.catcom.2008.02.016.

[36] Uddin MJ, Alam MM, Islam MA, Snigda SR, Das S, Rahman MM, et al. Tailoring the photocatalytic reaction rate of a nanostructured TiO_2 matrix using additional gas phase oxygen. Int Nano Lett. 2013;3:16. doi: 10.1186/2228-5326-3-16.

[37] Liu H, Zhai H, Hu C, Yang J, Liu Z. Hydrothermal synthesis of In_2O_3 nanoparticles hybrid twins hexagonal disk ZnO heterostructures for enhanced photocatalytic activities and stability. Nanoscale Res Lett. 2017;12:466. doi: 10.1186/s11671-017-2233-3.

[38] Verma S, Tirumala Rao B, Jayabalan J, Rai SK, Phase DM, Srivastava AK, et al. Studies on growth of Au cube-ZnO core-shell nanoparticles for photocatalytic degradation of methylene blue and methyl orange dyes in aqueous media and in presence of different scavengers. J Env Chem Eng. 2019;7(4):103209. doi: 10.1016/j.jece.2019.103209.

[39] Liu H, Hu Y, Zhang Z, Liu X, Jia H, Xu B. Synthesis of spherical Ag/ZnO heterostructural composites with excellent photocatalytic activity under visible light and UV irradiation. Appl Surf Sci. 2015;355:644–52. doi: 10.1016/j.apsusc.2015.07.012.

[40] Rakibuddin M, Ananthakrishnan R. Porous ZnO/Co_3O_4 heteronanostructures derived from nano coordination polymers for enhanced gas sorption and visible light photocatalytic applications. RSC Adv. 2015;5:68117–27. doi: 10.1039/c5ra07799k.

[41] Yang J, Zhu H, Peng Y, Li P, Chen S, Yang B, et al. Photocatalytic performance and degradation pathway of rhodamine B with TS-1/C3 N4 composite under visible light. Nanomaterials. 2020;10(4):756. doi: 10.3390/nano10040756.

[42] Sharma S, Mittal A, Chauhan NS, Saini S, Yadav J, Kushwaha M, et al. Mechanistic investigation of RhB photodegradation under low power visible LEDs using a Pd-modified TiO_2/Bi_2O_3 photocatalyst: Experimental and DFT studies. J Phys Chem Solids. 2022;162:110510. doi: 10.1016/j.jpcs.2021.110510.

[43] Rajabi HR, Farsi M. Effect of transition metal ion doping on the photocatalytic activity of ZnS quantum dots: Synthesis, characterization, and application for dye decolorization. J Mol Catal A. 2015;399:53–61. doi: 10.1016/j.molcata.2015.01.029.

[44] Wang Z, Lai C, Qin L, Fu Y, He J, Huang D, et al. ZIF-8-modified $MnFe_2O_4$ with high crystallinity and superior photo-Fenton catalytic activity by Zn-O-Fe structure for TC degradation. Chem Eng J. 2020;392:124851. doi: 10.1016/j.cej.2020.124851.